

## Simulations of the effects of interannual and decadal variability on the clear-sky outgoing long-wave radiation spectrum

By HELEN E. BRINDLEY<sup>1\*</sup> and RICHARD P. ALLAN<sup>2</sup>

<sup>1</sup>*Blackett Laboratory, Imperial College, London, UK*

<sup>2</sup>*Met Office, Hadley Centre for Climate Prediction and Research, Bracknell, UK*

(Received 19 November 2002; revised 23 May 2003)

### SUMMARY

Using atmospheric profiles derived from the Hadley Centre atmosphere climate model version 3 (HadAM3) as input to a radiative transfer code, the sensitivity of the resolved spectrum of clear-sky outgoing long-wave radiation to both interannual and longer-term atmospheric variability has been analysed. A comparison of the simulated spectra with available observations from two satellite-based instruments indicates a reasonable match, although consistent differences are present. These may be explained by a combination of uncertainties in the atmospheric state, and in the relative calibration of the two instruments. Focusing on the simulations: if HadAM3 is forced by the observed sea surface temperature (SST) record alone, and long-term alterations in the well-mixed greenhouse gases are imposed in the radiance simulations, the changes seen within the major absorption bands are robust. Under a second scenario, where the effects of solar variability, volcanic aerosol, ozone changes and increases in the well-mixed greenhouse gases are also included in the forcing of HadAM3, the long-term profile changes tend to show an enhanced upper-tropospheric warming and low/mid-stratospheric cooling, with increased near-surface humidities compared to the SST-only case. However, the tropospheric response of the system, manifested in the spectral change pattern over the atmospheric window and water vapour bands, falls within the range of year-to-year variability.

KEYWORDS: Climatic variability and change Spectral signatures

### 1. INTRODUCTION

Several authors have suggested the possibility of using measurements of spectrally resolved outgoing long-wave radiation (OLR) as a means for monitoring the climatic state and detecting change (Goody *et al.* 1995; Iacono and Clough 1996). Others have used a modelling approach to investigate how the forcings (Kiehl 1986) and feedbacks (Slingo and Webb 1997) associated with climate change are manifested in the OLR spectrum. The recent comparison of data from the Interferometric Monitor for Greenhouse Gases (IMG) instrument with that from the Infrared Interferometer Spectrometer (IRIS) instrument (Harries *et al.* 2001, hereafter H2001) provided the first observational evidence of a link between increases in greenhouse gases and a change in the radiative forcing of the earth–atmosphere system.

The appeal of using the planetary radiation spectrum directly is fourfold: firstly, its high information content, both in terms of the vertical temperature structure, and in atmospheric constituent concentrations; secondly, the availability of excellent spatial and temporal coverage from earth observation satellites; thirdly, the absence of a requirement for complicated inversion techniques; and fourthly, its fundamental link to the earth's energy balance. Nonetheless, because of the length of the observational records used, the study outlined in H2001 was limited to a comparison between two discrete periods in time. Given the variability within the climate system on all time-scales, it could be argued that high-frequency events may have influenced the magnitude of the signal reported.

One candidate that might be expected to exert a large influence on the temperature and water vapour fields, and hence the OLR at any given point in time, is the El Niño Southern Oscillation (ENSO). This quasi-periodic phenomenon has been extensively

\* Corresponding author: Space and Atmospheric Physics Group, Blackett Laboratory, Imperial College, London SW7 2BW, UK. e-mail: h.brindley@ic.ac.uk

studied (e.g. Cane 1986) and exhibits its primary response within the tropical and subtropical Pacific Ocean. During a warm event, enhanced sea surface temperatures (SSTs) and low surface pressure anomalies are found over the eastern Pacific, resulting in a shift in the area of maximum convection from its usual position over the Indonesian region eastwards into the central Pacific. Conversely, during a cold event the convection over the Indonesian region is enhanced, with suppressed vertical motion over the eastern Pacific.

Here we describe simulations performed to investigate the amount of change that might be expected in the resolved clear-sky OLR over an interannual time-scale, thereby including fluctuations relating to ENSO cycles, as compared to that seen between two well separated snapshots in time. Section 2 introduces the IRIS and IMG instruments while the simulation methodology is described in section 3. In section 4 an indication of the typical level of agreement between the observations and simulations is provided, and the simulations are used to identify the mechanisms responsible for the spectral pattern of change seen. Section 5 then investigates the degree to which interannual variability may have affected this difference signal. The conclusions to be drawn from this study are presented in section 6.

## 2. OBSERVATIONAL DATASETS

### (a) *IRIS-D instrument*

Designed with the primary aim of improved atmospheric soundings, the IRIS-D Michelson interferometer measured the infrared emission spectrum of the earth between 400 and 1600  $\text{cm}^{-1}$ , with a nominal apodised spectral resolution of 2.8  $\text{cm}^{-1}$  (Hanel *et al.* 1972). This instrument, on board the sun-synchronous, near-polar-orbiting Nimbus 4 satellite, had a field of view of approximately 95 km diameter from a mean altitude of 1100 km. One interferogram was taken every 16 seconds, calibration being performed via views of a warm black-body target and cold space every fifteenth and sixteenth cycle, respectively. IRIS-D was operational from April 1970 to January 1971, although a reduction in data quality occurred from September 1970 onwards due to instrument 'smear'. Unacceptably high noise levels at wave numbers greater than 1400  $\text{cm}^{-1}$  also limits the useful spectral range of the data.

### (b) *IMG instrument*

Flown on the ADEOS\* 1 satellite, the principal mission of the IMG instrument was to enable improved retrievals of greenhouse gases. Like IRIS, IMG is a Fourier transform spectrometer, the spectral range covered by three bands with a total spread of 600 to 3030  $\text{cm}^{-1}$ , at a nominal resolution of 0.1  $\text{cm}^{-1}$  (Kobayashi and Komae-shi 1999). Placed in a sun-synchronous, near-polar orbit, with a mean altitude of 800 km, and field of view of area 64  $\text{km}^2$ , the instrument provided measurements from October 1996 to June 1997.

## 3. SIMULATION METHODOLOGY

Simulations of spectrally resolved clear-sky OLR were performed over two separate 27-month intervals (April 1969 to June 1971, and April 1996 to June 1998) centred on the operational periods of the IRIS and IMG instruments. As a basis for the calculations, pentad-mean profiles of temperature and humidity were generated by the Hadley Centre

\* ADvanced Earth Observing System.

TABLE 1. EXPERIMENTAL DESIGN

Label	Temperature and humidity profiles	Trace gases
Case A	SST-only HadAM3 scenario	No change in WMGG <sup>1</sup> and ozone
Case B	SST-only HadAM3 scenario	Changes in WMGG and ozone
Case C	All-forcings HadAM3 scenario	Changes in WMGG and ozone
A–B	Measures direct effect of WMGG and ozone on the $T_B$	
B–C	Measures ‘indirect’ effect of WMGG, ozone, solar and aerosol forcings on the temperature and water vapour profiles and hence the $T_B$ spectrum	

<sup>1</sup>Well-mixed greenhouse gases ( $\text{CO}_2$ ,  $\text{N}_2\text{O}$ ,  $\text{CH}_4$ , CFC11, CFC12).  
See text for other definitions.

atmosphere climate model version 3 (HadAM3, Pope *et al.* 2000), applying the standard resolution of  $2.5^\circ$  latitude  $\times$   $3.75^\circ$  longitude with 19 levels in the vertical.

Using a climate model rather than re-analyses offers a versatile approach in the analysis of interannual and decadal changes in OLR spectra because the sensitivity of the simulated climate to initial conditions and to different radiative forcings may be assessed. Two scenarios were undertaken, based upon the HadAM3 experiments described in Allan and Slingo (2002). In the first, designated ‘SST-only’, the model was forced by version 3.1 of the observed Global sea-Ice and Sea Surface Temperature dataset (GISST, Rayner *et al.* 1996). Climatological aerosol and seasonally varying zonal-mean ozone concentrations were applied. For the second scenario, designated ‘all-forcings’, in addition to the GISST data, forcings due to changes in greenhouse gas concentrations, tropospheric and stratospheric ozone, direct and indirect sulphate aerosol effects, volcanic aerosol and yearly fluctuations in solar irradiance were prescribed. The details of these forcing scenarios are described in Johns *et al.* (2003). The climate-model simulations were initialized using output from previous experiments of a similar specification which were integrated from 1865 to the present day (Sexton *et al.* 2001). Four realizations of the SST-only scenario were produced, each being initialized from a different ensemble member of the Sexton *et al.* experiments beginning prior to the start of the 27-month simulations. This allowed an assessment of the model sensitivity to initial conditions. A single all-forcings experiment was produced.

For each SST-only realization, monthly mean surface temperatures and corresponding temperature and specific-humidity profiles were constructed from the pentad data and used as input to the MODTRAN3.7 (Berk *et al.* 1989) radiative-transfer code, in order to generate monthly mean clear-sky radiance spectra at  $1 \text{ cm}^{-1}$  resolution from  $600\text{--}1400 \text{ cm}^{-1}$ . For the all-forcing case the effects of ozone and the well mixed greenhouse gases (WMGG),  $\text{CO}_2$ ,  $\text{N}_2\text{O}$ ,  $\text{CH}_4$ , and the chlorofluorocarbons 11 and 12 (CFC11 and CFC12) were also accounted for. The latter were allowed to alter in time and location in line with observed records (Conway *et al.* 1994; Dlugokencky *et al.* 1994; Prinn *et al.* 1994) extrapolated to the requisite periods. Zonal monthly mean stratospheric ozone concentrations for each period were estimated using measured trends (Randel and Wu 1999) extrapolated back to 1970. Tropospheric ozone changes at the same temporal and spatial resolution were taken from calculations made using a three-dimensional chemical-transport model forced by realistic emission scenarios (Olivier *et al.* 1996). For ease of notation, in the following sections the term ‘trace gas’ refers to the combined effect of the WMGG and ozone. Finally, one further set of simulations was carried out, using the SST-only temperature and water vapour profiles but imposing the long-term trace gas increases in the radiative transfer code. Table 1 gives a summary

of the simulations performed, along with the insights that each can provide, and for each experiment assigns a case label used henceforward in the text.

In all cases the simulated radiances were degraded to the IRIS resolution using a Hamming window (Hanel *et al.* 1970), and converted to equivalent brightness temperatures,  $T_B$ . To reduce the computational time required to generate the  $T_B$  spectra, the horizontal resolution of both sets of input data was reduced to  $5^\circ$  latitude by  $5^\circ$  longitude. The effects of using a monthly mean profile rather than pentad mean data was investigated. If a  $T_B$  difference spectrum is being considered, the error due to averaging is less than  $\pm 0.4$  K across the  $600\text{--}1400\text{ cm}^{-1}$  wave number range.

#### 4. SPECTRA OF $T_B$ DIFFERENCES BETWEEN 1997 AND 1970

In order to aid interpretation of the difference spectra presented throughout this paper, the simulated effects of perturbations to surface temperature ( $T_{\text{sfc}}$ ), atmospheric temperature ( $T$ ) and atmospheric specific humidity ( $q$ ) on the spectrally resolved OLR are shown in Figs. 1(a)–(c), respectively. In each case the impact on OLR is expressed in terms of the change in top of the atmosphere brightness temperature,  $\Delta T_B$ , due to the given perturbation, from that obtained using the  $30^\circ\text{N}$  to  $30^\circ\text{S}$  average profile for April 1997.

Figure 1(a) was constructed by increasing  $T_{\text{sfc}}$  in steps of 0.5 K from the control value and calculating the corresponding  $\Delta T_B$ . As expected, the  $T_B$  response is confined to the relatively transparent window region from  $\sim 800\text{--}1250\text{ cm}^{-1}$ . Since the rate of change of  $T_B$  with  $T_{\text{sfc}}$  at a particular wave number is governed by the atmospheric transmissivity, the spectral variation of the  $T_B$  change becomes more pronounced with increasing  $T_{\text{sfc}}$ .

The impact on  $T_B$  of increasing the temperature by 5 K in each atmospheric layer in turn is illustrated in Fig. 1(b). The vertical response at a given wave number is determined by the transmission gradient or weighting function. Hence, in less absorbing regions such as the window, the maximum effect is seen when near-surface temperatures are perturbed. Conversely, in strongly absorbing regions, such as the centre of the  $667\text{ cm}^{-1}$   $\text{CO}_2$  band, the largest response occurs when stratospheric temperatures are increased.

Finally, the influence of layer-wise increments in  $q$  can be seen in Fig. 1(c). For consistency with Fig. 1(b) the increase applied in each layer was set equal to that required to keep relative humidity with respect to water constant given a 5 K temperature perturbation. The vertical distribution of the applied change is shown in Fig. 2. Low-level increases in  $\text{H}_2\text{O}$  result in enhanced continuum absorption across the window. At higher levels  $T_B$  is reduced via absorption and re-emission by the wing of the  $6.3\text{ }\mu\text{m}$   $\text{H}_2\text{O}$  vibration–rotation band. Over the spectral range under consideration the effects of water vapour changes above  $\sim 150\text{ mb}$  are not apparent.

Moving on to the observations themselves, given the observational lifetimes of IRIS and IMG instruments the only months that can be compared without introducing a seasonal bias are April to June (AMJ). Figure 3 shows the observed (a) IRIS, and (b) IMG mean AMJ clear-sky  $T_B$  spectra, and in (c) the associated IMG–IRIS difference, averaged over the tropical oceans between  $30^\circ\text{N}$  and  $30^\circ\text{S}$ . Corresponding simulated clear-sky spectra from case C are shown in grey. Whilst simulated clear-sky values were calculated diagnostically for all grid points, cloudy spectra were removed from the observations using the double threshold approach detailed in H2001. Therefore systematic sampling biases relating to the clear-sky sampling or to cloud contamination of the observations may arise. In particular, in contrast to the clear-sky satellite observations,

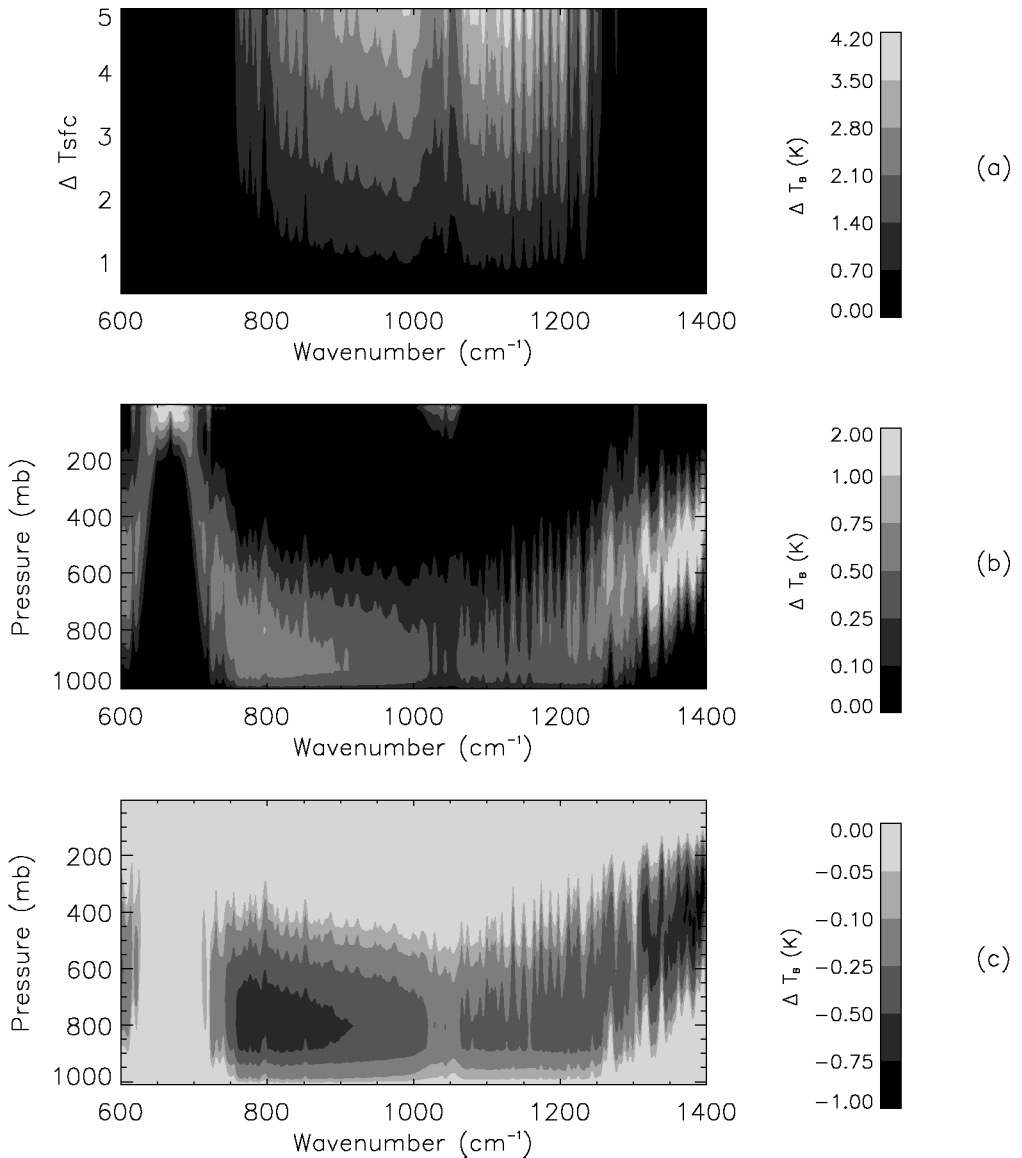


Figure 1. Sensitivity of the simulated top of the atmosphere brightness temperature ( $T_{\text{B}}$ ) spectrum for April 1997 over the tropical oceans to increases in: (a) surface temperature,  $T_{\text{sfc}}$ ; (b) atmospheric temperature,  $T$ ; and (c) specific humidity,  $q$ .

the simulated monthly mean spectra include contributions from moist, convective profiles. This would be expected to result in an underestimation of the total clear-sky OLR in the simulations (Cess and Potter 1987), and an overestimation of humidity-induced variability.

Comparing Figs. 3(a) and (b), the simulations generally show a better match with the IMG observations than with the IRIS measurements, particularly across the 750 to 1000  $\text{cm}^{-1}$  region. As noted in H2001, this may be due to the presence of residual cirrus cloud within the ‘clear’ IRIS spectra. However, the feature is seen consistently at all

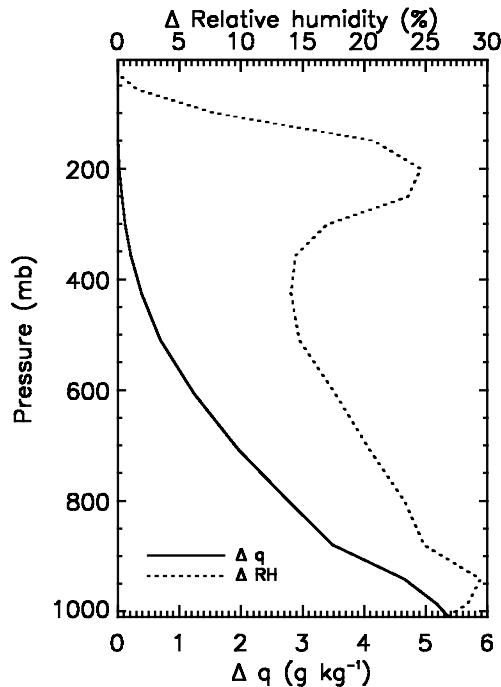


Figure 2. Vertical profile of the change in specific humidity ( $q$ ) and relative humidity used to construct Fig. 1(c).

locations for all the months studied, which could suggest the presence of an undetected calibration error (Hanel *et al.* 1972); this possibility will be explored in more detail in a future study. In Fig. 3(b), the slight overestimate in simulated  $T_B$  values across the entire window from  $750\text{--}1250\text{ cm}^{-1}$  compared to IMG is likely to be due to the use of a sea surface emissivity value of unity in the radiance simulations. Note that although this emissivity was spectrally invariant, including its spectral variation in the simulations has a minimal effect on the shape of the window response.

Further differences seen in the  $1060\text{ cm}^{-1}$   $\text{O}_3$  band and at the centre of the  $667\text{ cm}^{-1}$   $\text{CO}_2$  band can be explained by the fact that the uppermost level of HadAM3 is set at  $\sim 4\text{ mb}$ , so that top of the atmosphere brightness temperature will always be underestimated in these spectral regions.

At wave numbers greater than  $1300\text{ cm}^{-1}$ , the simulations underestimate  $T_B$  compared to both instruments. At these wave numbers the effects of mid- to upper-tropospheric relative humidity begin to dominate (Fig. 1(c)), and the use of monthly mean profiles will result in an underestimate of the outgoing  $T_B$  because of the nonlinear relationship between relative humidity and  $T_B$  (e.g. Geer *et al.* 1999). However, as the effect is present in both the 1970 and 1997 periods, the simulated IMG–IRIS  $T_B$  difference (Fig. 3(c)) is not significantly affected. Given this, the larger (less negative) differences seen in the simulations could be indicative of an underestimate of mid- to upper-tropospheric relative humidity in the later (IMG) period. If this were temperature related it would be consistent with the reduced spectral variation seen in the simulated differences across the wing of the  $\text{CO}_2$  band from  $680\text{ to }740\text{ cm}^{-1}$ , and the smaller signal seen in the Q branch of  $\text{CH}_4$  at  $1302\text{ cm}^{-1}$  (Fig. 1(b)). The underestimate in

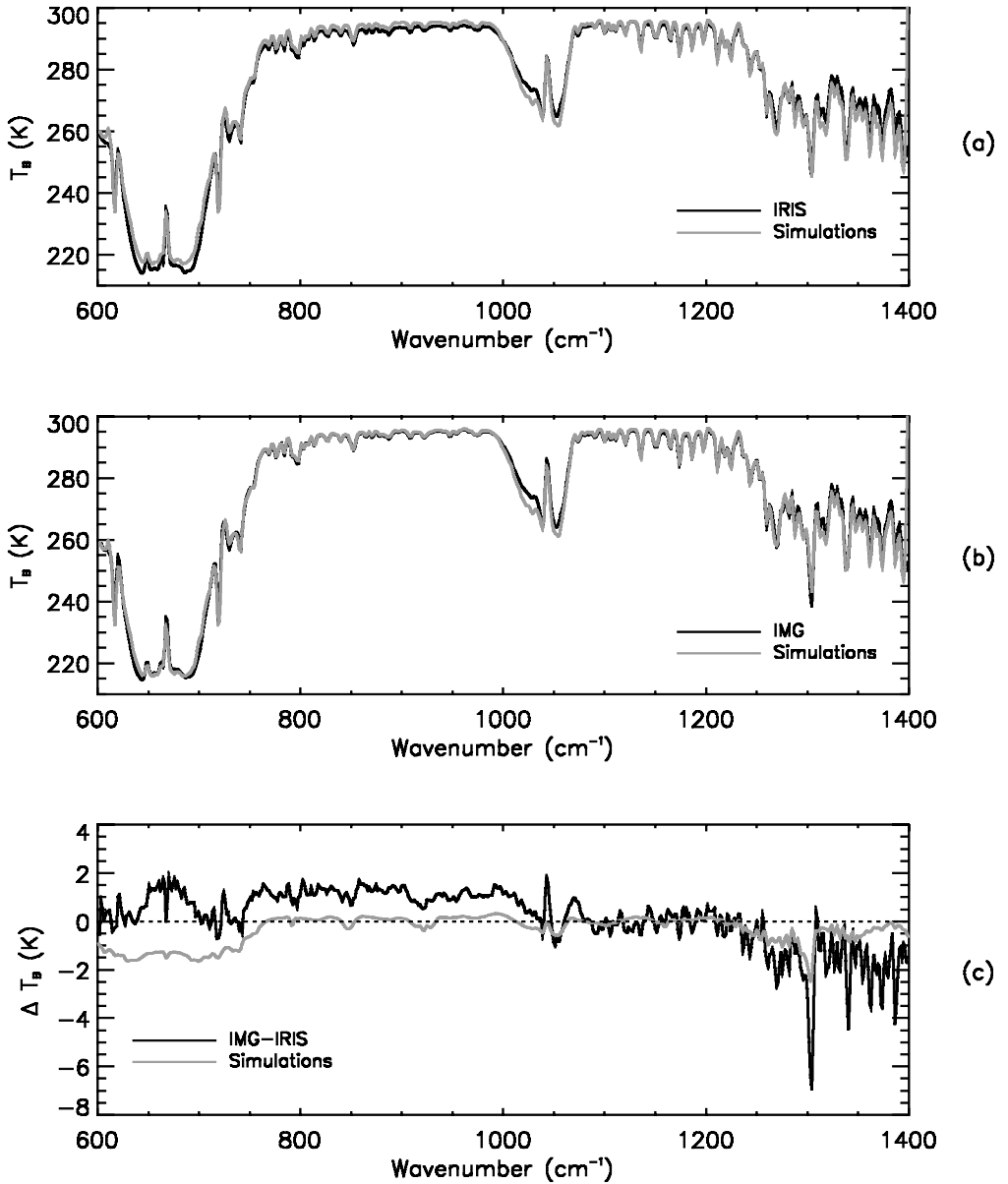


Figure 3. Observed (black) and simulated (grey) clear-sky atmosphere brightness temperature ( $T_B$ ) spectra averaged over the tropical oceans from 30°N to 30°S over April to June 1997–70 from: (a) the Infrared Interferometer Spectrometer (IRIS) instrument; (b) the Interferometric Monitor for Greenhouse Gases (IMG) instrument; (c) IMG-IRIS.

simulated  $T_B$  at wave numbers influenced by relative humidity would be reinforced by the sampling strategy employed in constructing the simulated and observed clear-sky spectra. As noted above, since all model grid point profiles are included, the simulations sample moist, cloudy regions of high relative humidity and hence low  $T_B$  compared to the ‘clear-sky’ observations. Further insight into the impact of sampling will be provided in section 5.

The availability of a number of different model realizations allows the separation of signals due to direct and indirect forcings within the spectral OLR. From case A, the first question to be asked is to what extent can SST and water vapour variations alone influence the resolved radiance change; cases B and C can then be used to investigate the impact of additional forcings on the climatic response.

In the following unless stated otherwise, differences refer to the seasonal mean AMJ  $T_B$ ,  $T$ , or  $q$  averages for 1997 minus the same parameter for 1970; for brevity they are referred to as 1997–1970 differences or changes.

### (a) SST and $H_2O$ induced changes

Figures 4(a)–(c) show the mean 1997–1970 changes in  $T$  and  $q$  for the tropical oceans from 30°N–30°S, averaged over the four realizations associated with case A. Given the potential influence of ENSO on the atmospheric state, the changes seen over two smaller regions centred on the equatorial east Pacific (10°N–10°S; 215–270°E) and west Pacific (10°N–10°S; 160–215°E) are also shown (Figs. 4(d)–(i); note change in scales). The grey shading in each case indicates the one standard deviation ( $1\sigma$ ) spread in the mean values.

Over the tropical oceans the model shows a relatively constant warming of  $\sim 0.2$  K at all tropospheric levels. At the tropopause a distinct cooling is apparent, with little change seen throughout the stratosphere (Fig. 4(a)). A very similar pattern is seen in the west Pacific (Fig. 4(d)) although the magnitude of the changes is larger, the tropospheric warming increasing from  $\sim 0.4$  K at the surface to a maximum of  $\sim 0.9$  K at 300 mb with an associated stronger tropopause cooling. In the east Pacific (Fig. 4(g)), the profile shape is slightly altered. Here, the maximum increase in temperature is located in the lower troposphere, with a surface warming of  $\sim 1.1$  K. Specific humidity changes are consistent with the temperature fields. Moistening occurs throughout the lower atmosphere in all locations, the increments in the two equatorial Pacific regions being larger than the tropic-wide increase (Figs. 4(b), (e) and (h)). The largest difference between the two equatorial Pacific regions is seen below 800 mb, with significantly enhanced moistening in the eastern Pacific. This pattern of behaviour might be expected from the classical ENSO picture, since the 1997–1970 difference effectively compares a warm ENSO state (1997) to a neutral one (1970) (e.g. Trenberth 1997; McPhaden 1999). Finally, changes in relative humidity are shown in Figs. 4(c), (f) and (i). Tropic-wide changes below 600 mb are small, and show a large variation between realizations. Between 600 and 300 mb all the realizations show a consistent increase of up to 1% before relaxing back to near-zero values at  $\sim 250$  mb (Fig. 4(c)). Over the equatorial Pacific regions, although the inter-realization spread is non-negligible, an increase of a few percent in relative humidity between 800 and 300 mb is seen in all realizations for both locations (Figs. 4(f) and (i)).

The associated mean 1997–1970  $T_B$  difference spectra,  $\Delta T_B$ , for all three locations are presented in Fig. 5. The shading indicates the spread in the differences obtained at the  $1\sigma$  level. Since the SST progression is identical in all four realizations, the greatest spread would be expected in those spectral regions which are more sensitive to the overlying atmosphere, particularly those additionally influenced by water vapour. This is borne out by the increasingly large  $\sigma$  at wave numbers greater than  $1300\text{ cm}^{-1}$ . However, it can clearly be seen that the spectral shape of the  $\Delta T_B$  pattern is robust to changes in HadAM3 initial conditions. Although not shown explicitly, the spread due to variations in the initial conditions has a similar spectral pattern and magnitude in all the  $\Delta T_B$  spectra presented from here onward.

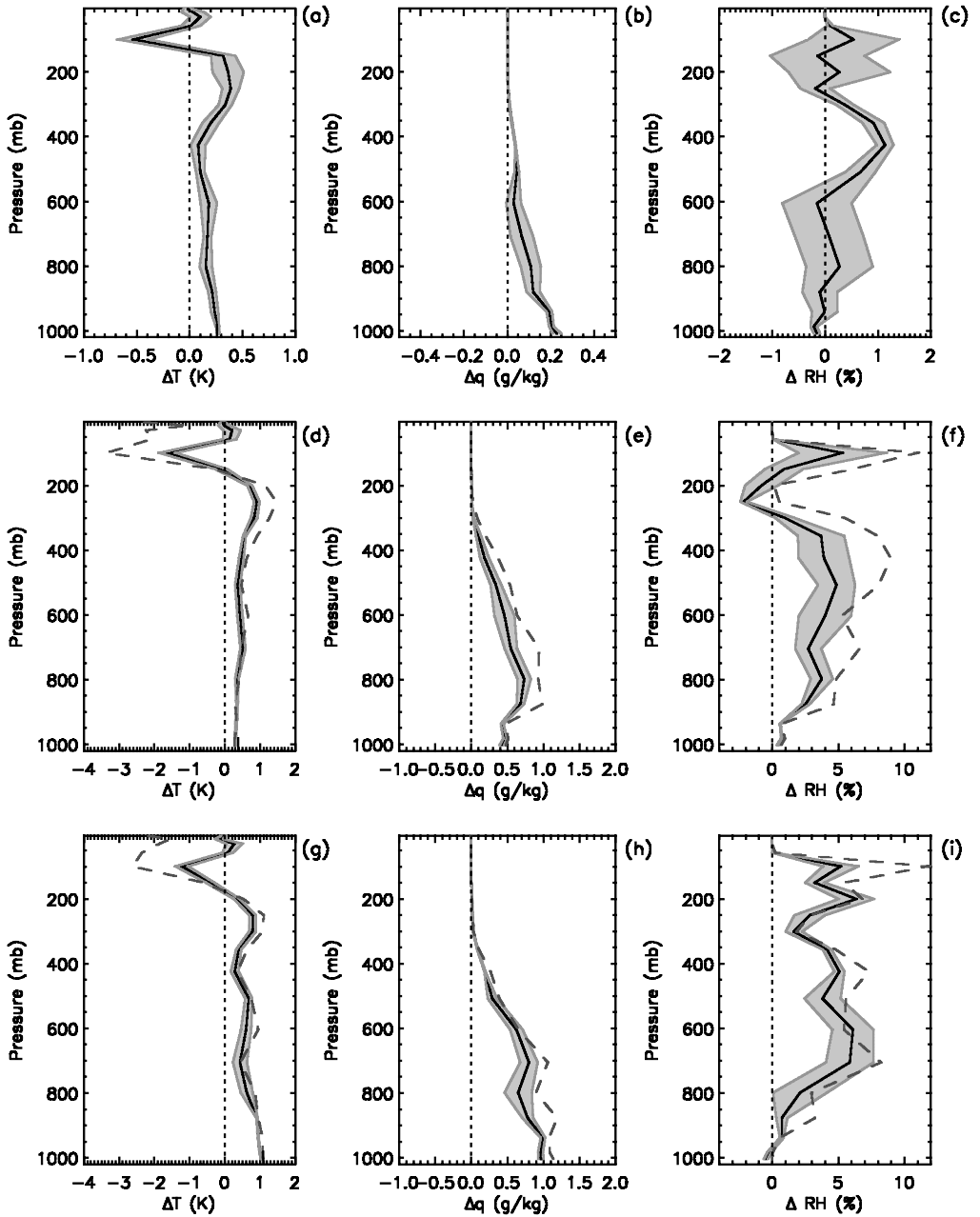


Figure 4. Changes between April to June 1997 and April to June 1970 of profiles of atmospheric temperature ( $T$ ), specific humidity ( $q$ ) and relative humidity ( $RH$ ) for the tropical oceans and equatorial west and east Pacific regions. In each case the solid lines and shading shows results from the HadAM3 (see text) model simulations forced by sea surface temperatures only with associated one standard deviation uncertainties: (a) tropical  $\Delta T$ ; (b) tropical  $\Delta q$ ; (c) tropical  $\Delta RH$ ; (d) west Pacific  $\Delta T$ ; (e) west Pacific  $\Delta q$ ; (f) west Pacific  $\Delta RH$ ; (g) east Pacific  $\Delta T$ ; (h) east Pacific  $\Delta q$ ; and (i) east Pacific  $\Delta RH$ . In (d) to (i) the dashed lines show the changes seen under the all-forcing scenario.

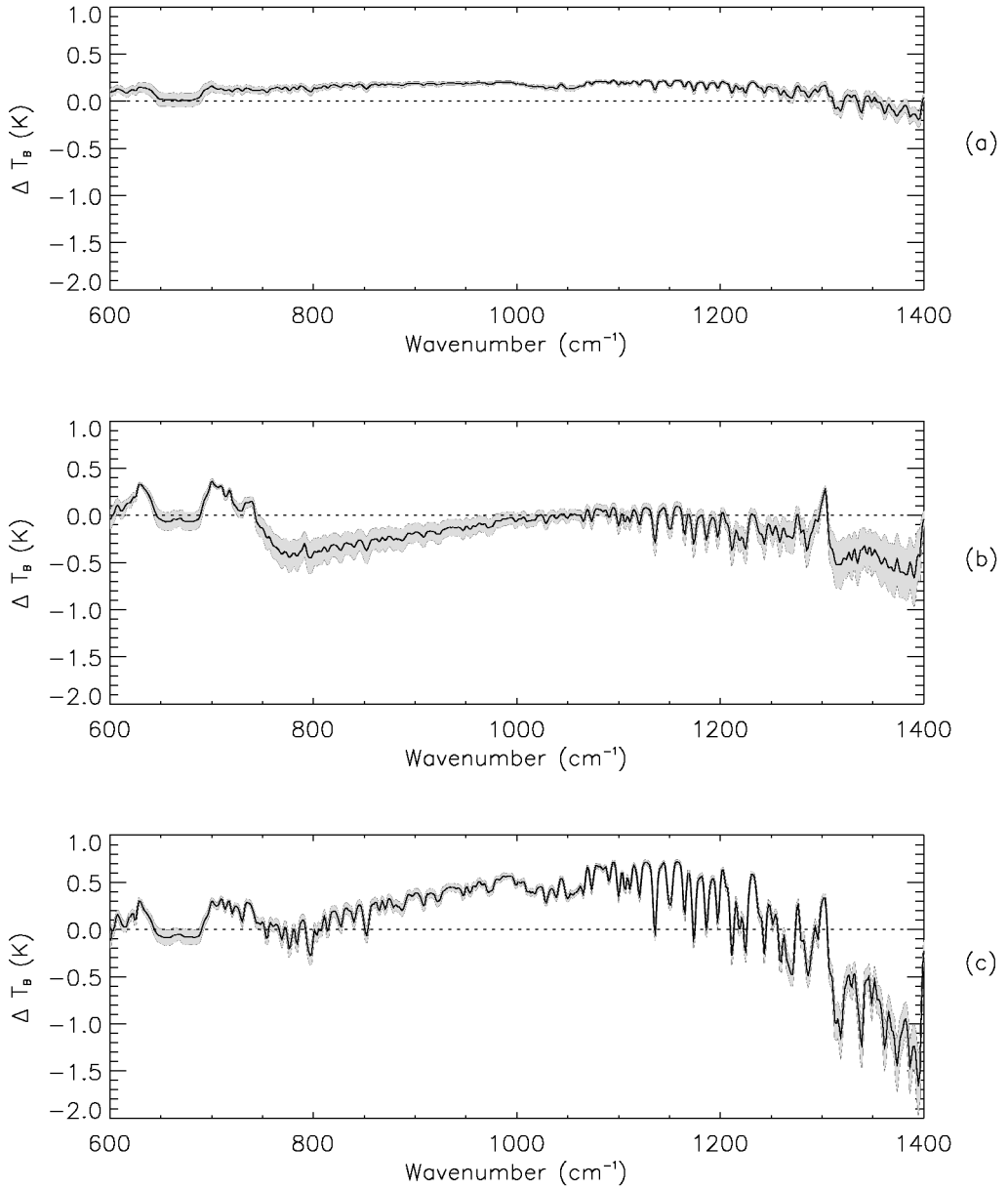


Figure 5. Spectral April to June brightness temperature differences ( $\Delta T_B$ ) between 1997 and 1970 over: (a) tropical oceans; (b) the equatorial west Pacific; and (c) the equatorial east Pacific, using HadAM3 (see text) model simulations forced by sea surface temperature changes only and with no trace gas changes imposed (case A, see Table 1). Uncertainties in the differences of one standard deviation are shaded.

Over the tropical oceans (Fig. 5(a))  $\Delta T_B$  is relatively flat, the small positive values over the window region being a reflection of an increase in  $T_{sfc}$  of 0.26 K from 1970 to 1997. The negative  $T_B$  differences at wave numbers greater than  $1350 \text{ cm}^{-1}$  are a manifestation of the small increase in relative humidity seen at  $\sim 400 \text{ mb}$  (Fig. 4(c)). In the west Pacific (Fig. 5(b)) the effects of the increase in lower-tropospheric  $q$  (Fig. 4(e)) are sufficient to overwhelm the increase in  $T_B$  associated with the surface and lower-tropospheric warming (Fig. 4(d)) leading to a negative  $T_B$  change across the window. A similar effect is seen in the wing of the  $\nu_2$  water vapour waveband (i.e. wavelength  $\nu > 1250 \text{ cm}^{-1}$ ). In this case, the increase in mid/upper-tropospheric water vapour more than counteracts the increases in temperature at the same levels. Since the remaining trace gas concentrations are held constant, in those spectral regions dominated by trace gas absorption the temperature change is clearly reflected. Particular examples include the wing of the  $\nu_2$   $\text{CO}_2$  band ( $700 < \nu < 750 \text{ cm}^{-1}$ ), and the centre of the  $\nu_2$   $\text{CH}_4$  band ( $\nu \sim 1302 \text{ cm}^{-1}$ ), where the enhanced  $T_B$  is indicative of the rise in upper-tropospheric temperatures.

In contrast to the west Pacific, in the east Pacific a positive  $T_B$  change is seen across the window (Fig. 5(c)). Here the surface warming, though strongly modulated by the increase in lower-tropospheric  $q$  (as indicated by the depth of the absorption lines between  $1100$  and  $1200 \text{ cm}^{-1}$ ), is more than sufficient to compensate. The other major change from the western side of the basin occurs at wave numbers greater than  $1250 \text{ cm}^{-1}$  where the enhanced increase in mid/upper-level relative humidity is manifested in the marked reduction in  $T_B$ .

### (b) *Effects of trace gas changes*

The east and west Pacific  $\Delta T_B$  spectra observed when representative trace gas changes are included in the radiance simulations (case B) are shown in Fig. 6(a). Since the SST and  $\text{H}_2\text{O}$  changes are identical to those in case A, the only alterations in the  $\Delta T_B$  spectra are seen within the trace gas absorption bands. This is illustrated by Fig. 6(b) which shows the difference between the case B and case A spectra of  $\Delta T_B$  (in the sense B–A) for the east Pacific. The effect of the increase in the well-mixed gases from 1970 to 1997 is to shift the peak emitting level higher in the atmosphere. In regions sounding primarily the troposphere (e.g.  $\text{CH}_4$   $\nu_2$  band,  $\text{CO}_2$   $\nu_2$  band wings) this results in a reduction in  $\Delta T_B$ , with the converse being true for those regions more sensitive to stratospheric temperatures (e.g.  $\text{CO}_2$   $\nu_2$  band centre). For ozone, the effects of an increase in lower/mid-stratospheric concentration (not shown) tend to result in an increase in local thermal emission, but a reduction in the near-surface radiation reaching space. In this case the latter effect has a larger impact, so that the  $\Delta T_B$  values are reduced across the  $\nu_3$   $\text{O}_3$  band (centred at  $1042 \text{ cm}^{-1}$ ).

For an insight into the effects of both trace gas and external forcings on the spectrally resolved  $T_B$ , Fig. 7(a) shows the east and west Pacific  $\Delta T_B$  spectra for case C. To aid interpretation, the dashed lines in Figs. 4(d)–(i) illustrate the changes seen in the atmospheric profiles of  $T$  and  $q$  for this case. The major long-term effect across the equatorial Pacific is the reduction of stratospheric temperatures by  $\sim 2 \text{ K}$ , and the enhancement of upper-tropospheric temperatures by up to  $\sim 0.5 \text{ K}$ . Nearer the surface the controlling influence of the SST fields means that the changes seen in all three cases are similar. The specific-humidity response is interesting since, despite the lack of deviation between cases seen in the lower-level temperature field, specific-humidity increases are somewhat larger in case C. By differencing the  $\Delta T_B$  spectra obtained from cases B and C, the influence of the effects of the additional forcings present in case C on the temperature and humidity profiles can be identified in the radiative response.

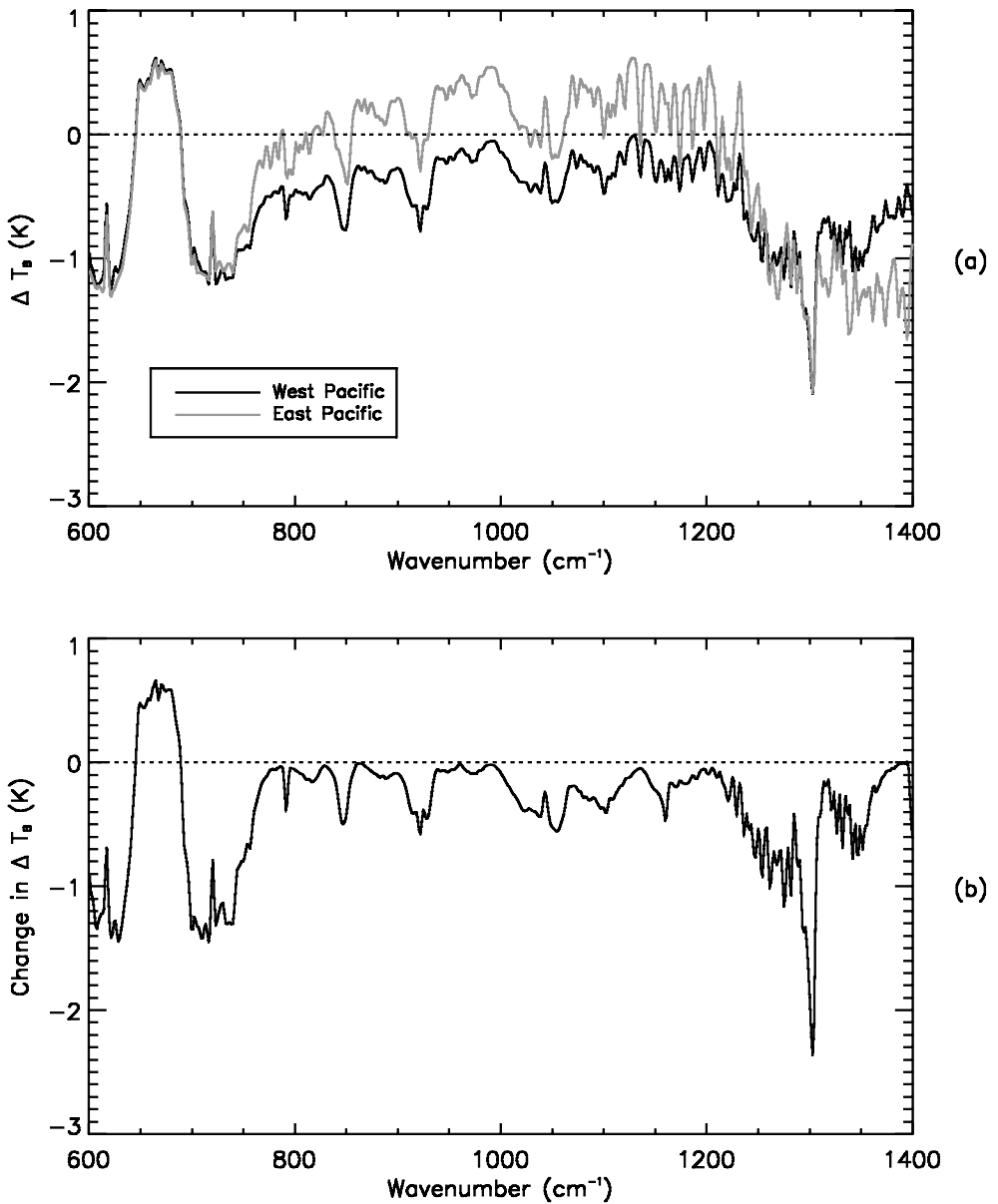


Figure 6. (a) Spectral April to June brightness temperature differences ( $\Delta T_B$ ) between 1997 and 1970 over the west and east Pacific using HadAM3 (see text) model simulations forced by sea surface temperature changes only but with trace gas changes imposed (case B, see Table 1); (b) similar, but change in  $\Delta T_B$  between case B and case A over the east Pacific.

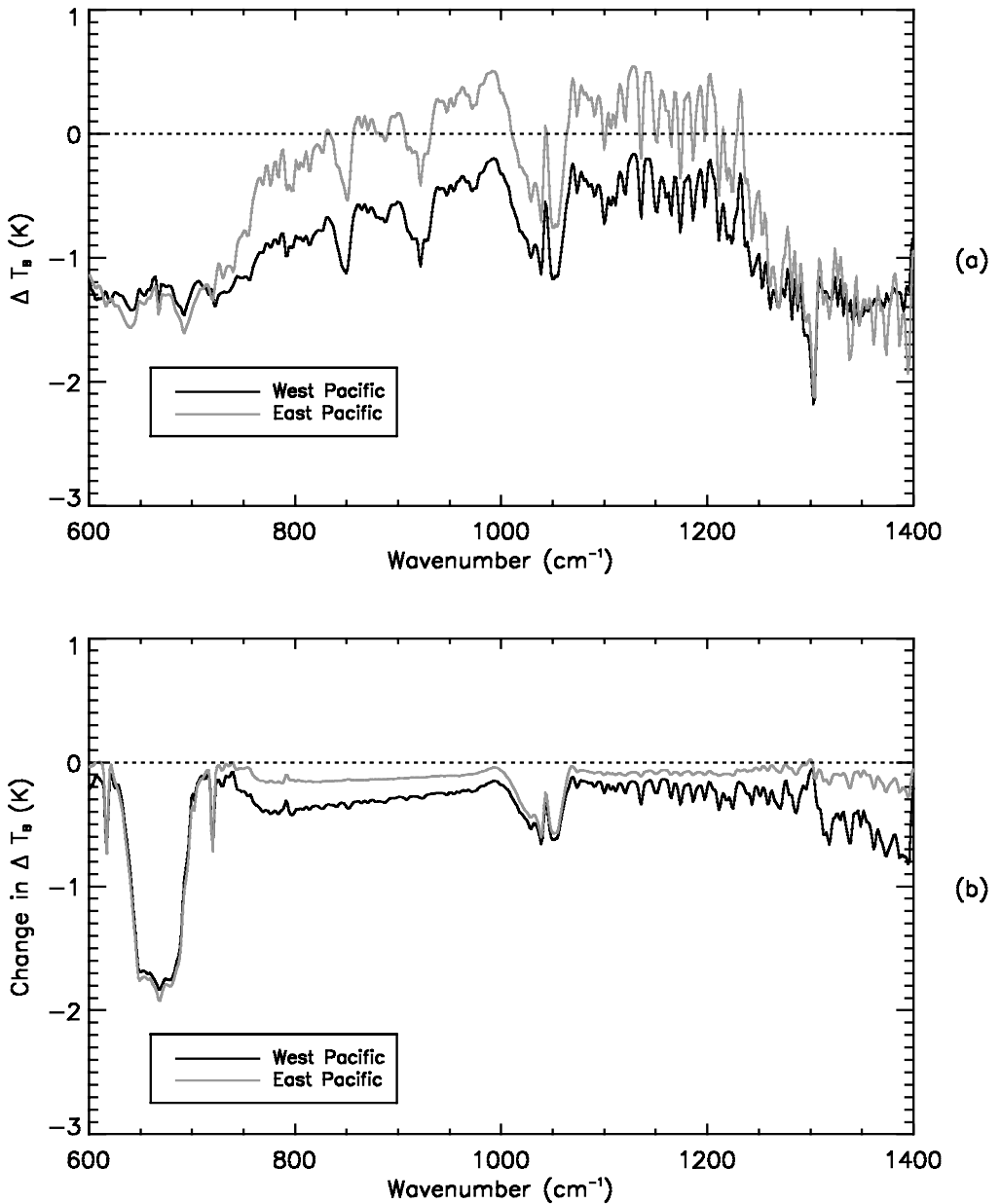


Figure 7. (a) As Fig. 6(a) but using HadAM3 simulations with all forcings included and trace gas changes imposed (case C); (b) as Fig. 6(b) but comparing cases C and B.

Figure 7(b) shows that the humidity increases tend to overwhelm the temperature rises in the window and in the  $\text{H}_2\text{O } \nu_2$  band wing across the Pacific, whereas the stratospheric temperature reductions result in markedly reduced emissions over the  $\nu_3 \text{ O}_3$  and  $\nu_2 \text{ CO}_2$  bands.

The results shown in Figs. 5 to 7 suggest that, although the atmospheric response to SST forcing alone can account for much of the simulated  $T_B$  change, the inclusion of trace gas and external forcings when generating the atmospheric temperature and

humidity fields does exert a marked extra influence throughout the spectral range under consideration. It is also apparent that the direct effect of trace gas increases has the dominant role in determining the  $T_B$  change in many regions of the spectrum.

### 5. INTERANNUAL VARIABILITY IN DIFFERENCE FIELDS

Since the HadAM3 simulations provide 3-years worth of AMJ data over each epoch, an estimate of the robustness of the 1997–1970 changes in tropical  $\Delta T_B$  signal can be obtained. Results are again presented for the tropical oceans as a whole but, instead of focusing on the equatorial regions highlighted in the previous section, two alternative zones designated ‘convective’ and ‘subsidence’ are utilized. The two areas are selected according to their fractional cloud cover,  $f_c$ , over each month. Areas of high fractional cover ( $f_c > 0.75$ ) tend to be associated with convective activity, whilst small cloud fractions ( $f_c < 0.15$ ) indicate subsidence. Sub-sampling in this way should ensure that the results are not affected by seasonal movements in large-scale circulations, and provide an insight into how spectrally resolved OLR and its variability are influenced by different dynamical regimes. Note that the precise thresholds chosen are rather arbitrary, but the results obtained are robust to a reasonable perturbation to either value. For succinctness, again only results for AMJ seasonal means are presented, but the findings for individual months are similar.

The 1997–1970 AMJ long-term changes in the vertical temperature profiles over the selected regions are shown in Figs. 8(a), (d) and (g) for case C. The grey shading represents the range of interannual variability, while the vertical bars cutting the  $x$ -axis indicate the long-term SST changes. Corresponding differences in the specific-humidity structure are given in the second column of the figure, with the resulting  $\Delta T_B$  spectra presented in the third. Considering first the tropical oceans (Figs. 8(a)–(c)), over the troposphere the 27-year temperature change falls within the range of differences seen from year-to-year. Changes in tropospheric relative humidity show similar behaviour. In the stratosphere there is a distinct separation between the long-term temperature response and interannual differences, with the former showing a strong O<sub>3</sub>- and CO<sub>2</sub>-induced cooling. The interannual variability seen in the tropospheric temperature and humidity structure is reflected in the fact that the long-term spectral pattern of change does not emerge from the short-term differences across the window and within the water vapour band wing. However, the effects of long-term increases in the WMGG are clearly distinct from interannual perturbations in the gas concentrations. The stratospheric cooling noted previously is manifested as a reduction in  $T_B$  across the O<sub>3</sub>  $\nu_3$  band and the centre of the CO<sub>2</sub>  $\nu_2$  band.

Sub-sampling the tropical oceans into subsidence and convective zones results in the difference profiles seen in Figs. 8(d) and (e), and (g) and (h), respectively. In each case the number of points retained varies from between 18 and 60 out of a possible 660 according to month and year. For the subsidence case, the long-term temperature difference suggests a reduction in temperatures in the lowest atmospheric levels followed by an increase in the mid/upper-tropospheric lapse rate with time. This results in lower  $T_B$  across the window, coupled with a steeper gradient between 725 and 775  $\text{cm}^{-1}$  (Fig. 8(f)). The reduced upper-tropospheric temperature is also apparent as a larger negative  $T_B$  difference over the 1302  $\text{cm}^{-1}$  CH<sub>4</sub> band. Changes in tropospheric relative humidity show the opposite behaviour to the temperature profile (Fig. 8(e)). Low- to mid-level reductions result in the distinct peaks seen at wave numbers between 1140–1200  $\text{cm}^{-1}$ , whilst the increase in upper-tropospheric values results in stronger negative-going lines within the wing of the H<sub>2</sub>O band at wave

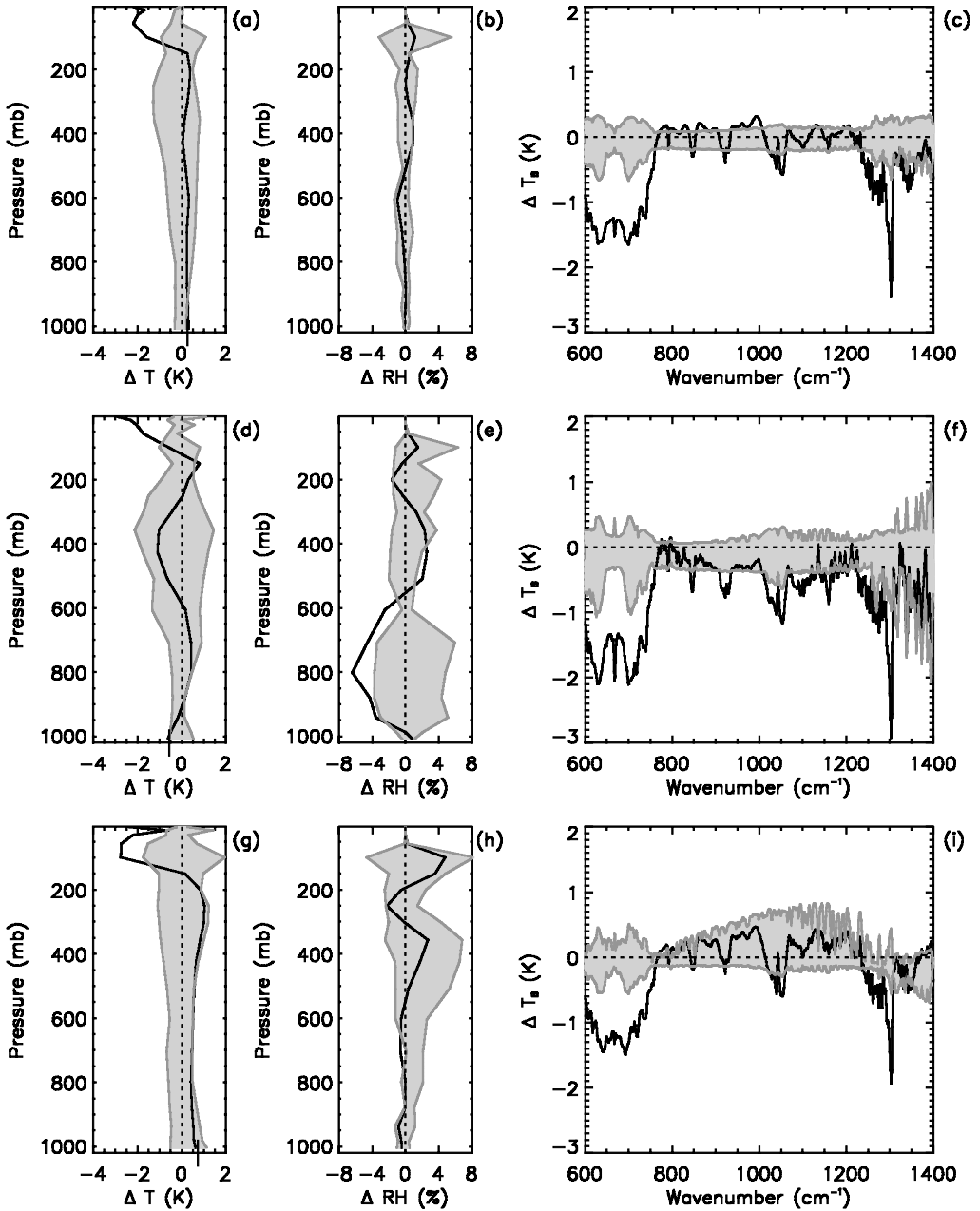


Figure 8. Profiles of April to June differences between 1997 and 1970 for the tropical oceans of: (a) temperature ( $T$ ); (b) relative humidity ( $RH$ ); and (c) the associated brightness temperature differences ( $\Delta T_B$ ) spectra (from case C, see Table 1). The grey shading represents the range of interannual variability in each case. (d), (e) and (f) as (a), (b) and (c) but for subsidence zones; (g), (h) and (i) as (a), (b) and (c) but for convective zones.

numbers greater than  $1300\text{ cm}^{-1}$ . Comparing these findings to the differences seen between the observed and simulated difference spectra in Fig. 3(c), indicates that selecting spectra generated from nominally 'clear' profiles does improve the level of agreement between simulations and observations. In contrast, the convective case shows a similar long-term pattern of behaviour to the tropical mean, albeit with slightly larger difference magnitudes. Indeed, despite the fact that sub-sampling produces a larger long-term change in the temperature and humidity profiles, the associated range of interannual variability is also increased. Hence, in terms of the spectral response, only the WMGG and ozone signals are distinct from interannual differences.

## 6. CONCLUSIONS

Motivated by the recent comparison of IRIS and IMG data for AMJ 1970 with those for AMJ 1997, we have utilized temperature and humidity information from an ensemble of HadAM3 runs to assess the sensitivity of clear-sky brightness temperature spectra to a variety of atmospheric forcings. In addition, the relative magnitudes of the spectral signatures of short-term variability, compared with changes seen over the 27-year time-scale have been investigated.

Through AMJ 1997 the climate was entering a strong warm ENSO event; conversely in 1970 the picture was more typical of neutral conditions. Simulated  $T_B$  spectra generally show reasonable agreement with the available spectral observations, although consistent differences are discernible. These may be explained by a combination of uncertainties in the atmospheric state and in the relative calibration of the two instruments. Sub-sampling the simulations into subsidence zones tends to improve the agreement with the observations. However, there is still some evidence to suggest a larger increase in free-tropospheric humidity in the observations than in the simulations by considering the  $T_B$  reductions over the water vapour band ( $\nu > 1300\text{ cm}^{-1}$ ), and the lack of a consistent temperature signal in the wing of the  $\nu_2$   $\text{CO}_2$  band and  $\text{CH}_4$  band centre.

When forced purely by observed SSTs, over the equatorial Pacific the modelled 1997–1970 difference shows enhanced warming and low-level moistening on the eastern side of the basin, compared to smaller increases in the west. From the radiance simulations, corresponding  $T_B$  difference fields indicate that the eastern near-surface warming is sufficient to result in enhanced window emission. On the western side, over the same spectral region, increased absorption by low-level water vapour dominates. Imposing trace gas changes in the radiance simulations leads to reduced emission within the given absorption bands.

If additional forcings due to greenhouse gases,  $\text{O}_3$ , solar activity and volcanic aerosols are included in the HadAM3 runs, the major effect on the atmospheric profile is to introduce a strong low/mid-stratospheric cooling, consistent with enhanced  $\text{CO}_2$  and depleted stratospheric  $\text{O}_3$  concentrations. The profiles also indicate an additional upper-tropospheric warming and lower-level moistening over the equatorial Pacific compared to the SST-only case. Some caution must be attached to the significance of these latter differences, since an assessment of the sensitivity of the profiles to small changes in the initial conditions in the all-forcing experiment has not been attempted. However, if the sensitivity were similar to that seen in the SST-only case, the deviation between the two scenarios would be robust. In terms of the corresponding  $T_B$  spectra, the inclusion of extra forcings does exert a marked influence, with reduced emissions over the entire spectral range under consideration compared to the SST-only scenario.

The availability of two sets of 3 years of model data centred on the IRIS and IMG observational periods allowed the generation of interannual as well as long-term

difference spectra. Our analysis shows that although there are spectral regions where a long-term change in the climatic state is distinguishable from short-term variability, over much of the spectrum the latter effect dominates. As anticipated in H2001, the forcing signatures seen in the WMGG absorption bands are distinct from patterns seen on interannual time-scales. In addition, the stratospheric temperature response to the inclusion of increases in CO<sub>2</sub> concentration and stratospheric ozone depletion emerges from the range of year-to-year variability and is clearly seen in the spectral patterns of change. Nevertheless, in all the cases considered the long-term tropospheric response of the system, manifested over the atmospheric window and within the water vapour absorption bands, is firmly within the envelope of interannual variability. Therefore a much longer, well calibrated and well sampled spectral dataset is required to extract the information on subtle changes in water vapour, temperature and cloud that relate to climate feedback processes.

## ACKNOWLEDGEMENTS

We thank Professor Anthony Slingo, Professor John Harries and Dr Jacqui Russell for their assistance in interpreting the data and improving the manuscript, and an anonymous reviewer for further helpful suggestions. H. Brindley was funded by the Met Office under Agreement No. Met 1b/2861. R. Allan was supported by the UK Department for Environment, Food and Rural Affairs contract, PECD 7/12/37.

## REFERENCES

- Allan, R. P. and Slingo, A. 2002 Can current climate forcings explain the spatial and temporal signatures of decadal OLR variations? *Geophys. Res. Lett.*, **29**(7), 1141, doi: [10.1029/2001GL014620](https://doi.org/10.1029/2001GL014620)
- Berk, A., Bernstein, L. and Robertson, D. 1989 MODTRAN: 'A moderate resolution model for LOWTRAN 7'. AFGL-TR-88-0177, US Air Force Geophysics Laboratory, Hanscom Air Force Base, Mass., USA
- Cane, M. 1986 El Niño. *Ann. Rev. Earth Planet. Sci.*, **14**, 43–70
- Cess, R. and Potter, G. 1987 Exploratory studies of cloud radiative forcing with a general circulation model. *Tellus A*, **39**, 460–473
- Conway, T., Tans, P. and Waterman, L. 1994 'Atmospheric CO<sub>2</sub> records from sites in the NOAA/CMDL air sampling network'. Pp. 41–49 in *Trends '93: A compendium of data on global change*. Eds. T. Boden, D. Kaiser, R. Sepanski and F. Stoss. ORNL/CDIAC-65. Carbon Dioxide Information Analysis Center, Oak Ridge National Laboratory, Oak Ridge, Tennessee, USA
- Dlugokencky, E., Lang, P., Masarie, K. and Steele, L. 1994 'Atmospheric CH<sub>4</sub> records from sites in the NOAA/CMDL air sampling network'. Pp. 274–350 in *Trends '93: A compendium of data on global change*. Eds. T. Boden, D. Kaiser, R. Sepanski and F. Stoss. ORNL/CDIAC-65. Carbon Dioxide Information Analysis Center, Oak Ridge National Laboratory, Oak Ridge, Tennessee, USA
- Geer, A., Harries, J. and Brindley, H. 1999 Spatial patterns of climate variability in upper-tropospheric water vapor radiances from satellite data and climate model simulations. *J. Climate*, **12**, 1940–1955
- Goody, R., Haskins, R., Abdou, W. and Chen, L. 1995 Detection of climate forcing using emission spectra. *Earth Observation and Remote Sensing*, **13**, 713–722
- Hanel, R., Schlachman, B., Clark, F., Prokesh, C., Taylor, J., Wilson, W. and Chaney, L. 1970 The Nimbus 3 Michelson interferometer. *Appl. Opt.*, **9**, 1767–1774
- Hanel, R., Conrath, B., Kunde, V., Prabhakara, C., Revah, I., Salomonson, V. and Welford, G. 1972 The Nimbus 4 infrared spectroscopy experiment: 1. Calibrated thermal emission spectra. *J. Geophys. Res.*, **77**, 2629–2641

- Harries, J., Brindley, H., Sagoo, P. and Bantges, R. 2001 Increases in greenhouse forcing inferred from the outgoing long-wave spectra of the earth in 1970 and 1997. *Nature*, **410**, 355–357
- Iacono, M. and Clough, S. 1996 Application of infrared spectrometer clear sky spectral radiance to investigations of climate variability. *J. Geophys. Res.*, **101**, 29439–29460
- Johns, T. C., Gregory, J. M., Ingram, W. J., Johnson, C. E., Jones, A., Lowe, J. A., Mitchell, J. F. B., Roberts, D. L., Sexton, D. M. H., Stevenson, D. S., Tett, S. F. B. and Woodage, M. J. 2003 Anthropogenic climate change for 1860 to 2100 simulated with the HadCM3 model under updated emissions scenarios. *Clim. Dyn.*, **20**, 583–612, doi: 10.1007/s00382-002-0296-y
- Kiehl, J. 1986 Changes in the radiative balance of the atmosphere due to increases in CO<sub>2</sub> and trace gases. *Adv. Space Res.*, **6**, 55–60
- Kobayashi, H., and Komae-shi, (Eds.), 1999 'Interferometric monitor for greenhouse gases'. IMG Project Technical Report. IMG Mission Operation and Verification Committee, Tokyo, Japan
- McPhaden, M. 1999 Genesis and evolution of the 1997–98 El Niño. *Science*, **283**, 950–954
- Olivier, J., Bouwman, A., Maas, W., Berdowski, J., Veldt, C., Bloos, J., Visschedijk, A., Zandveld, P. and Haverlag, J. 1996 'Description of EDGAR Version 2.0: A set of global emission inventories of greenhouse gases and ozone-depleting substances for all anthropogenic and most natural sources on a per country basis and on a 1 deg × 1 deg grid'. RIVM report number 771060 002 and TNO-MEP report number R96/119. National Institute of Public Health and the Environment, Bilthoven, the Netherlands
- Pope, V., Gallani, M., Rowntree, P. and Stratton, R. 2000 The impact of new physical parameterisations in the Hadley Centre climate model: HadAM3. *Clim. Dyn.*, **16**, 123–146
- Prinn, R., Weiss, R., Alyea, F., Cunnold, D., Fraser, P., Simmonds, P., Crawford, A., Rasmussen, R. and Rosen, R. 1994 'Atmospheric CFC-11 (CC13F), CFC-12 (CC12F2), and N<sub>2</sub>O from the ALE/GAGE network'. Pp. 396–420 in *Trends '93: A compendium of data on global change*. Eds. T. Boden, D. Kaiser, R. Sepanski and F. Stoss. ORNL/CDIAC-65. Carbon Dioxide Information Analysis Center, Oak Ridge National Laboratory, Oak Ridge, Tennessee, USA
- Randel, W. and Wu, F. 1999 A stratospheric ozone trends data set for global modeling studies. *Geophys. Res. Lett.*, **26**, 3089–3092
- Rayner, N., Horton, E., Parker, D., Folland, C. and Hackett, R. 1996 'Version 2.2 of the Global sea-Ice and Sea Surface Temperature dataset, 1903–1994'. Climate Research Technical Note 74, Hadley Centre, Met Office, Bracknell, UK
- Sexton, D., Rowell, D., Folland, C. and Karoly, D. 2001 Detection of anthropogenic climate change using an atmospheric GCM. *Clim. Dyn.*, **17**, 669–685,
- Slingo, A. and Webb, M. 1997 The spectral signature of global warming. *Q. J. R. Meteorol. Soc.*, **123**, 293–307
- Trenberth, K. 1997 The definition of El Niño. *Bull. Am. Meteorol. Soc.*, **78**, 2771–2777